

Frustrated magnetic planes with intricate interaction pathways in the mineral langite $\text{Cu}_4(\text{OH})_6\text{SO}_4 \cdot 2\text{H}_2\text{O}$

Stefan Lebernegg,^{1,*} Alexander A. Tsirlin,^{2,3} Oleg Janson,⁴ Günther J. Redhammer,⁵ and Helge Rosner^{1,†}

¹*Max Planck Institute for Chemical Physics of Solids, Nöthnitzer Str. 40, 01187 Dresden, Germany*

²*National Institute of Chemical Physics and Biophysics, 12618 Tallinn, Estonia*

³*Experimental Physics VI, Center for Electronic Correlations and Magnetism,*

Institute of Physics, University of Augsburg, 86135 Augsburg, Germany

⁴*Institute of Solid State Physics, Technical University Vienna,*

Wiedner Hauptstr. 8–10/138, 1040 Vienna, Austria

⁵*Department of Materials Sciences & Physics, University Salzburg, Hellbrunnerstr. 34, 5020 Salzburg, Austria*

(Dated: December 7, 2024)

Magnetic and crystallographic properties of the mineral langite $\text{Cu}_4(\text{OH})_6\text{SO}_4 \cdot 2\text{H}_2\text{O}$ are reported. Its layered crystal structure features a peculiar spatial arrangement of spin- $\frac{1}{2}$ Cu^{2+} ions that arises from a combination of corner- and edge-sharing chains. Experimentally, langite orders antiferromagnetically at $T_N \simeq 5.7$ K as revealed by magnetization and specific heat measurements. Despite this very low energy scale of the magnetic transition, langite features significantly stronger couplings on the order of 50-70 K. Half of the Cu^{2+} spins are weakly coupled and saturate around 12 T, where the magnetization reaches $0.5 \mu_B/\text{Cu}$. These findings are rationalized by density-functional band-structure calculations suggesting a complex interplay of frustrated exchange couplings in the magnetic planes. A simplified model of coupled magnetic sublattices explains the experimental features qualitatively. To start from reliable structural data, the crystal structure of langite in the 100–280 K temperature range has been determined by single-crystal x-ray diffraction, and the hydrogen positions were refined computationally.

PACS numbers: 75.50.Ee, 75.10.Jm, 71.20.Ps, 61.50.Ks

I. INTRODUCTION

Low-dimensional magnets show unique diversity of crystal structures and associated spin lattices, where a plethora of quantum phenomena can be observed.^{1–3} The physics of quantum spin chains has been actively explored in Cu^{2+} compounds featuring chains of corner- or edge-sharing CuO_4 plaquette units. The corner-sharing geometry results in uniform spin chains with a negligibly small second-neighbor coupling, as in Sr_2CuO_3 ,^{4,5} AgCuVO_4 ⁶ and $\text{KCuMoO}_4(\text{OH})$.⁷ The edge-sharing geometry is by far more common. It gives rise to competing nearest-neighbor and next-nearest-neighbor couplings, where the former (J_1) is typically ferromagnetic, while the latter (J_2) is antiferromagnetic. Such $J_1 - J_2$ frustrated spin chains develop incommensurate spin correlations and helical magnetic order,^{8,9} although few instances of ferromagnetic intrachain spin order are known as well.^{10,11} The helical spin arrangement observed in simple binary compounds CuCl_2 ¹² and CuBr_2 ¹³ and in more complex materials like linarite $\text{PbCu}(\text{OH})_2\text{SO}_4$,¹⁴ all being frustrated $J_1 - J_2$ spin chains, may trigger electric polarization induced by the magnetic order, thus leading to multiferroic behavior.^{15–17}

One may naturally ask what happens when two types of spin chains, those with edge- and corner-sharing geometries, are placed next to each other within one material. Spin systems comprising several magnetic sublattices with different dimensionalities and energy scales may have very unusual low-temperature properties. The sublattices are, to a certain extent, independent, hence

two magnetic transitions manifesting the ordering within each of the sublattices can be observed. On the other hand, the ordering within one sublattice will necessarily depend on the other sublattice, because three-dimensional (3D) long-range order typically involves interactions between the sublattices. Unusual manifestations of quantum order-from-disorder have been observed in $\text{Sr}_2\text{Cu}_3\text{O}_4\text{Cl}_2$ ^{18–22} featuring interpenetrating square lattices with drastically different exchange couplings. In CuP_2O_6 , where square planes of spins- $\frac{1}{2}$ coexist with uniform spin chains, very strong spin fluctuations are observed even below the Néel temperature T_N , and the value of T_N is unusually low for a quasi-two-dimensional (2D) antiferromagnet.²³ The coexistence of corner- and edge-sharing Cu^{2+} chains could be even more interesting because of the different nature of spin correlations, which are expected to be antiferromagnetic collinear and helical, for the corner- and edge-sharing chains, respectively.

The coexistence of the edge- and corner-sharing geometries is very common for Cu^{2+} minerals. In antlerite²⁴ and szenicsite,²⁵ one edge-sharing chain is encompassed by two corner-sharing chains that together form a three-leg spin ladder. The edge- and corner-sharing chains can also form infinite layers, as in deloryite $\text{Cu}_4(\text{UO}_2)(\text{MoO}_4)_2(\text{OH})_6$,²⁶ derriksite $\text{Cu}_4(\text{UO}_2)(\text{SeO}_3)_2(\text{OH})_6$,²⁷ niedermayrite $\text{Cu}_4\text{Cd}(\text{SO}_4)_2(\text{OH})_6$,²⁸ and langite $\text{Cu}_4(\text{OH})_6\text{SO}_4 \cdot 2\text{H}_2\text{O}$. The crystal structure of the latter mineral is shown in Fig. 1. Layers of alternating edge- and corner-sharing chains (Fig. 1, right) are well separated by SO_4 sulphate groups and water molecules. A somewhat similar

structure without water molecules has been reported for the mineral brochantite $\text{Cu}_4(\text{OH})_6\text{SO}_4$ ^{29,30} that, however, features a much smaller interlayer separation, hence substantial interlayer couplings can be expected. In this paper, we focus on the magnetism of langite, because sufficiently pure natural samples of this mineral are available, and individual structural planes should be very weakly coupled magnetically.

The paper is organized as follows: Applied experimental and theoretical methods are described in Sec. II. The crystal structure of langite including the single-crystal data collected at low temperatures and hydrogen positions determined computationally is presented in Sec. III. Sec. IV provides experimental results on thermodynamic properties of langite. The electronic band structure and computed exchange coupling constants are discussed in Sec. V. Eventually, a detailed discussion and summary are given in Secs. VI and VII, respectively.

II. METHODS

All experiments have been performed on a natural sample (Fig. 1) of langite from the Podlipa and Reiner mine, Lubietova, Slovakia. The sample quality was first thoroughly controlled by laboratory powder X-ray diffraction (XRD) (Huber G670 Guinier camera, $\text{CuK}\alpha_1$ radiation, ImagePlate detector, $2\theta = 3 - 100^\circ$ angle range).

Single-crystal X-ray diffraction between 100 and 280 K was performed on a Bruker SMART APEX CCD-diffractometer equipped with a Cryostream liquid nitrogen low-temperature device. A single crystal, selected on the basis of its optical properties (sharp extinctions, regular shape and homogeneity in color) was glued on top of a glass capillary (0.1 mm). Intensity data were collected with graphite-monochromatized $\text{MoK}\alpha$ radiation (50 kV, 30 mA). The crystal-to-detector distance was 40 mm and the detector was positioned at $-28^\circ 2\theta$ using an ω -scan mode strategy at four different φ -positions (0° , 90° , 180° and 270°). 630 frames with $\Delta\omega = 0.3^\circ$ were acquired for each run. The 3D data were integrated and corrected for Lorentz polarization and background effects using the APEX2 software (Bruker – Nonius, 2004). Structure solution (using Patterson methods) and subsequent weighted full-matrix least-square refinements on F^2 were done with SHELXL-97³¹ as implemented in the program suite WinGX 1.64.³²

Magnetization measurements were done on a Quantum Design (QD) SQUID MPMS in magnetic fields up to 5 T and using the vibrating sample magnetometer (VSM) setup of Quantum Design PPMS up to 14 T in the temperature range of 1.6–300 K. Heat capacity data were acquired with the QD PPMS in fields up to 14 T.

Electronic structure calculations within density functional theory (DFT) were performed with the full-potential local-orbital code FPL09.07-41³³ on the 100 K crystal structure in combination with the local density approximation (LDA),³⁴ generalized gradient approxi-

mation (GGA)³⁵ and the DFT+ U method.^{36,37} A $4 \times 4 \times 4$ k -mesh was employed for LDA and GGA runs while super cells used for DFT+ U calculations were computed for about 100 k -points in the symmetry-irreducible part of the first Brillouin zone. We also performed auxiliary calculations using the Heyd-Scuseria-Ernzerhof (HSE06) hybrid DFT-functional³⁸ as implemented in the Vienna Ab initio Simulation Package (VASP5.2) code.³⁹

The hydrogen positions, which are essential for the calculation of the exchange couplings,^{40,41} have not been determined so far⁴² since H is almost invisible in XRD due to its very low scattering power. Alternative experimental techniques such as neutron diffraction require large and, preferably, deuterated samples that are not available in nature. Therefore, we determined the positions of hydrogen by numerical optimization of the atomic parameters with respect to a minimization of the total energy. These calculations were performed within GGA and have proved to be highly efficient and sufficiently accurate for cuprates in recent studies.^{40,41,43}

The exchange coupling constants J_{ij} were calculated within DFT following two different strategies. One strategy involves the analysis of the half-filled LDA bands at the Fermi level allowing for the determination of leading exchange pathways by an evaluation of the electron hopping integrals t_{ij} . The t_{ij} are computed as off-diagonal Hamiltonian matrix elements of Cu-centered Wannier functions (WFs) constructed for the half-filled bands. The spurious metallic state produced for magnetic insulators within LDA can be remedied by inserting LDA-based t_{ij} into an effective Hubbard model with the effective onsite Coulomb repulsion U_{eff} , where in cuprates typically $U_{\text{eff}} \simeq 4.5$ eV.^{23,40,43} In the limit of strong correlations, $t_{ij} \ll U_{\text{eff}}$, which is perfectly fulfilled in langite (see Table II), antiferromagnetic (AFM) contributions to the total exchange constants J_{ij} can be estimated in second order as $J_{ij}^{\text{AFM}} = 4t_{ij}^2/U_{\text{eff}}$. A more detailed description of the procedure can be found, e.g., in Refs. 40 and 44.

Alternatively, strong electron correlations are added on top of LDA by the LSDA+ U method in a mean-field way and are thus included in the self-consistent procedure. This allows for calculating total exchange constants $J_{ij} = J_{ij}^{\text{FM}} + J_{ij}^{\text{AFM}}$, which contain also the ferromagnetic (FM) contributions. A fully localized limit (FLL) approximation was used for correcting the double counting. The on-site Coulomb repulsion and Hund's exchange were set to $U_d = 8.5 \pm 1$ eV and $J_d = 1$ eV, respectively, a choice which has been successfully used for several other cuprates.^{40,43,45} The total exchange coupling constants J_{ij} of the spin Hamiltonian

$$\hat{H} = \sum_{\langle ij \rangle} J_{ij} \hat{S}_i \cdot \hat{S}_j \quad (1)$$

are calculated as differences between total energies of various collinear (broken-symmetry) spin states.^{13,43,46}

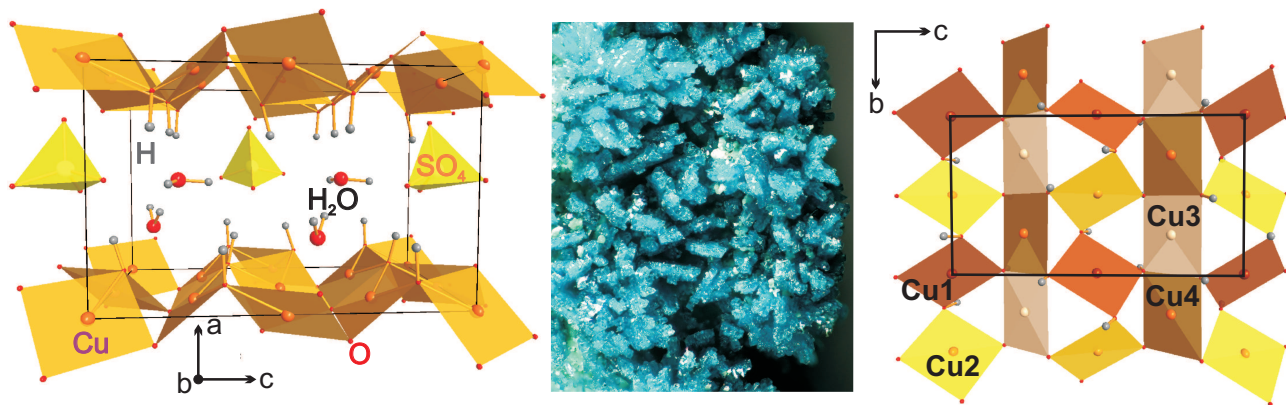


FIG. 1. (Color online) The left panel shows the crystal structure of langite. CuO_4 plaquettes are shown in orange, H are shown as grey spheres and SO_4 groups are shown in yellow. In the right panel, a single crystallographic layer is displayed where different colors for the four different Cu-positions are used. The picture in the center shows small light-blue langite crystals from the Podlipa and Reineria mine, Lubietova, Slovakia.

III. CRYSTAL STRUCTURE

Using the experimental crystal structure of langite reported in Ref. 42, we first routinely performed a DFT-optimization of the atomic parameters of all atoms in the unit cell with the lattice parameters being fixed to their experimental values. Deviations up to 0.3 Å between the experimental and optimized Cu–O bond lengths prompted us to reinvestigate the crystal structure of langite with single-crystal XRD. We also performed low-temperature XRD measurements in order to probe possible temperature-induced structural changes that may be relevant to understanding the magnetism.

Table I compiles the results of the structural study at 100 K, which served as input for all DFT calculations. Additional crystallographic data collected at 140, 220, 250, 280 K are provided in the Supplemental Material.⁴⁷ In the temperature range between 100–280 K the unit cell volume increases by about 0.9% with increasing T . The largest change in the lattice parameters was observed not along a perpendicular to the structural layers (Fig. 1), as one might intuitively expect, but along the c direction. With increasing T , the c parameter increases by about 0.35% arising reflecting the flattening of the layers. Changes along the a and b axes are similar, about 0.26% each. The monoclinic angle remains almost constant for the investigated temperature range.

Atomic positions of hydrogen, which have never been reported in the literature,⁴² are also given in Table I. They were obtained by GGA-optimization using tentative positions determined experimentally from single-crystal XRD data. When only hydrogen atoms were allowed to relax, the forces on the oxygen atoms of water molecules (OW1 and OW2) turned out to be quite large, while one of the hydrogen atoms moved towards the SO_4 group. Such a structure containing HSO_4 hydrosulfate groups would be quite unexpected and very different from that of the related Cu-sulphate mineral brochantite

$\text{Cu}_4(\text{OH})_6\text{SO}_4$, where neutron diffraction data reliably placed hydrogen atoms into the O–H groups linked to the Cu–O layers and not into the HSO_4 groups.²⁹ We, thus, relaxed the positions of all H atoms together with those of OW1 and OW2 and could stabilize the anticipated langite structure by 2.6 eV/unit cell, while the tentative HSO_4 configuration became energetically highly unfavorable. A full relaxation of all atomic positions further confirms the stability of the $\text{Cu}_4(\text{OH})_6\text{SO}_4 \cdot 2\text{H}_2\text{O}$ structure and shows no signatures of the HSO_4 groups.

Table I summarizes atomic positions in langite, including the OW1 and OW2 positions determined both experimentally and by the GGA-optimization. The difference between the experimental and computational positions of water molecules may reflect temperature-induced structural changes, because DFT yields the crystal structure at zero temperature, whereas experimental structure determination has been performed down to 100 K, only. However, we did not observe any sharp structural phase transitions below 100 K in thermodynamic properties reported in Sec. IV. It is also possible that the discrepancy between the experimental and computational positions of water molecules is intrinsic and related to marginal disorder, which is a plausible explanation, given the weak (hydrogen) bonding between the water molecules and the rest of the crystal structure. Vibration spectroscopy could provide further insight into the nature of hydrogen bonding and positions of water molecules in langite, but it lies beyond the scope of our study, which is focused on the magnetism of langite. Relevant magnetic interactions run within the Cu–O layers and should not depend on the exact positions of the out-of-plane water molecules. For the sake of consistency and given the fact that magnetic ordering in langite occurs well below 100 K, we used the relaxed positions of OW1 and OW2 in the further microscopic analysis (Sec. V).

The crystal structure of langite features four different Cu-positions. The basic building unit are layers formed

TABLE I. Refined atomic positions (in fractions of lattice parameters) and isotropic atomic displacement parameters U_{iso} (in $\times 10^{-2} \text{ \AA}^2$) of langite collected at 100 K. Refinement residuals are $R_1 = 4.64\%$, $wR_2 = 7.6\%$. All atoms are in the general position $2a$ of the space group $P1c1$. The lattice parameters are as follows: $a = 7.1231(8) \text{ \AA}$, $b = 6.0305(7) \text{ \AA}$, $c = 11.1935(12) \text{ \AA}$ and $\beta = 90.1479(14)^\circ$. OW and HW denote the O and H atoms of the H_2O molecules. The OS atoms belong to the SO_4 tetrahedra. The H-positions have been obtained by numerical optimization within GGA. For OW, experimental and optimized positions are provided.

Atom	x/a	y/b	z/c	U_{iso}
Cu1	0.99960(13)	0.99762(18)	0.49990(9)	0.46(2)
Cu2	0.99260(13)	0.49213(19)	0.50188(9)	0.43(3)
Cu3	0.00399(14)	0.75566(18)	0.75295(11)	0.40(2)
Cu4	0.00878(15)	0.25490(17)	0.75183(11)	0.38(2)
S	0.5778(4)	0.1854(3)	0.4201(3)	0.46(4)
O1	0.8860(9)	0.0001(10)	0.6634(6)	0.41(12)
O2	0.8882(9)	0.5044(10)	0.6652(6)	0.54(13)
O3	0.1156(9)	0.5098(10)	0.8432(7)	0.43(13)
O4	0.1412(8)	0.2452(11)	0.5604(6)	0.39(13)
O5	0.8600(8)	0.7441(9)	0.4412(6)	0.45(13)
O6	0.1256(9)	0.0054(10)	0.8398(7)	0.56(14)
OS1	0.7845(8)	0.2311(9)	0.4116(5)	0.42(12)
OS2	0.5388(8)	0.0666(9)	0.5344(6)	1.08(13)
OS3	0.4770(8)	0.4015(10)	0.4219(6)	0.94(12)
OS4	0.5165(8)	0.9519(10)	0.8163(6)	0.91(13)
OW1	0.2626(9)	0.7398(10)	0.6008(6)	0.73(13)
OW2	0.5178(9)	0.4283(11)	0.6955(7)	1.16(15)
GGA-optimization				
OW1	0.27422	0.73641	0.59891	
OW2	0.52514	0.43403	0.69849	
H1	0.27170	0.74411	0.03266	
H2	0.35870	0.38187	0.12901	
H3	0.72674	0.74906	0.46285	
H4	0.26599	0.00612	0.33549	
H6	0.74761	0.99558	0.65733	
H7	0.25162	0.46853	0.36133	
H1W1	0.51463	0.54313	0.28622	
H2W1	0.36074	0.85755	0.57697	
H1W2	0.51392	0.27508	0.68068	
H2W2	0.74644	0.49444	0.67040	

by planar chains of edge-sharing CuO_4 plaquettes (type A chain) as well as buckled chains of corner-sharing CuO_4 plaquettes (type B chains) (Fig. 1), where the chains are directly linked to each other. Sulphate groups and water molecules are located between the layers. The Cu–O–Cu bridging angles, which are of crucial importance for the exchange couplings between the Cu-sites, amount to $99.49^\circ/99.11^\circ$, $98.64^\circ/97.81^\circ$ in the type A chains and $101.05^\circ/104.71^\circ$ in the type B chains, respectively. The bridging angles between the two chain types, A and B,

are between $105\text{--}109^\circ$, i.e. the layers are strongly buckled (Fig. 1). According to Goodenough-Kanamori rules, one expects ferromagnetic (FM) exchange for bridging angles close to 90° and antiferromagnetic (AFM) exchange for larger bridging angles. The crossover is at about $95\text{--}100^\circ$,^{44,48} and the exchange couplings in the edge-sharing chains of langite are difficult to guess in this transition region, even qualitatively (see Sec. V), while all other couplings would naively be assumed AFM. However, such simple considerations are bound to fail for langite as will be demonstrated in Secs. V and VI below.

IV. THERMODYNAMIC PROPERTIES

All measurements presented in this section were performed on powder from the same specimen as the one used for the single-crystal XRD. The powder quality has been diligently checked by powder XRD, revealing almost pure langite.⁴⁷

The temperature-dependent magnetic susceptibility $\chi(T)$ measured in magnetic fields of 0.5 and 2 T is shown in Fig. 2, where the two curves are almost identical. A Curie-Weiss fit $\chi(T) = C/(T+\theta)$ of the high-temperature regime (220–290 K) of the 2 T data yields $\theta = 18.2$ K and $C = 0.481$ emu K (mol Cu)⁻¹. From the constant C , we obtain an effective magnetic moment of $1.96 \mu_B/\text{Cu}$ which is larger than the spin only value of 1.73 and implies the g -factor of 2.26 lying still in the expected range for Cu^{2+} compounds.^{29,40,49} The positive θ indicates predominant antiferromagnetic couplings, which are, however, quite weak. In the low-temperature regime, $\chi(T)$ features a rather sharp peak at 7.5 K. This peak is somewhat asymmetric and thus different from the susceptibility maxima in conventional low-dimensional antiferromagnets, where short-range magnetic order is formed well above the Néel temperature T_N .^{50,51} While no indications of a magnetic transition are seen in the raw susceptibility data, Fisher’s heat capacity $d(\chi T)/dT$ reveals a kink around 5.5 K that can be paralleled to the anomaly in the specific heat and ascribed to the magnetic ordering transition. The absence of a Curie tail at the lowest T , typically arising from paramagnetic spin-1/2 impurities (see e.g. Ref. 40), demonstrates the high quality of our natural sample.

The 5.7 K anomaly in the specific heat generally resembles a λ -type anomaly, which is expected at a second-order phase transition. The broadening of this anomaly may be driven by effects of magnetic anisotropy. Magnetic nature of the 5.7 K transition is corroborated by its field dependence. Despite the relatively low value of T_N , the transition is well visible up to at least 14 T, and the transition temperature changes only slightly in the applied magnetic field. At higher temperatures, the lattice contribution to the specific heat dominates. Below the transition temperature, $C_p(T)$ decreases, but it does not follow the simple T^3 behavior expected for a conventional 3D antiferromagnet.⁵² Layered systems like langite may

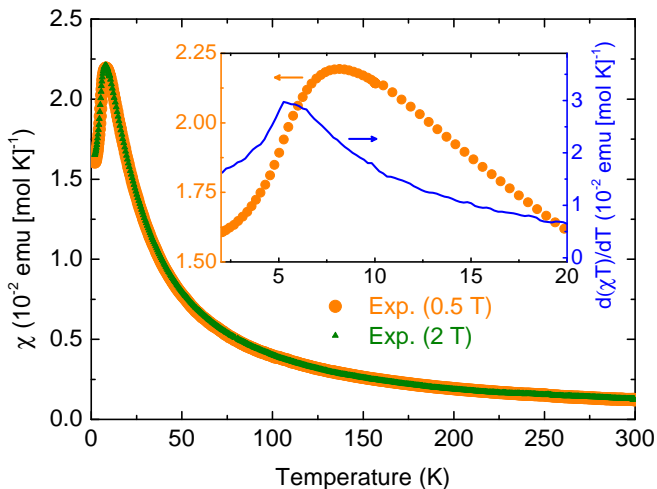


FIG. 2. (Color online) The experimental susceptibility data $\chi(T)$ collected at magnetic fields of 0.5 and 2.0 T. $d(\chi T)/dT$ is shown in the inset as blue line.

be close to the 2D regime with the T^2 temperature dependence of the specific heat⁵² that, however, was not observed either.

The magnetic contribution C_{mag} was obtained by subtracting the lattice contribution C_{lat} from the measured C_p data, where $C_{\text{lat}}(T)$ was approximated by fitting a polynomial⁴⁷ $C_{\text{lat}}(T) = \sum_{n=3}^{n=7} c_n T^n$, proposed by Johnston *et al.*,⁵³ to the $C_p(T)$ data in the temperature range of 20–39 K. In zero magnetic field, the magnetic entropy S_{mag} was estimated to about 6.7 J/(mol K) by integrating C_{mag}/T . Thus, only about 30% of the expected $S_{\text{mag}} = 4R \ln 2$ for a spin-1/2 system is released within the transition anomaly and right above T_N , while the rest is spread towards higher temperatures, which is typical for low-dimensional antiferromagnets⁵¹ and corroborates that T_N is somewhat lower than the energy scale of the exchange couplings given by, e.g., $\theta \simeq 18$ K. A similar value for S_{mag} has been reported for the related mineral brochantite (see also Sec. VI) releasing 7.9 J/(mol K), which is about 34% of the total magnetic entropy, in the vicinity of the magnetic transition.²⁹

Field-dependent magnetization $M(H)$ (Fig. 4) measured in fields up to 14 T features two kinks around 4 T, reaches half-saturation around 12 T, and keeps increasing up to at least 14 T. The kink at 4 T is reminiscent of a spin-flop transition that, however, happens at a much higher field than in other Cu^{2+} oxides.⁵⁴ Above 2 K, the features of the magnetization curve are smeared out, so we were not able to map them as a function of temperature and construct a comprehensive $T-H$ phase diagram.

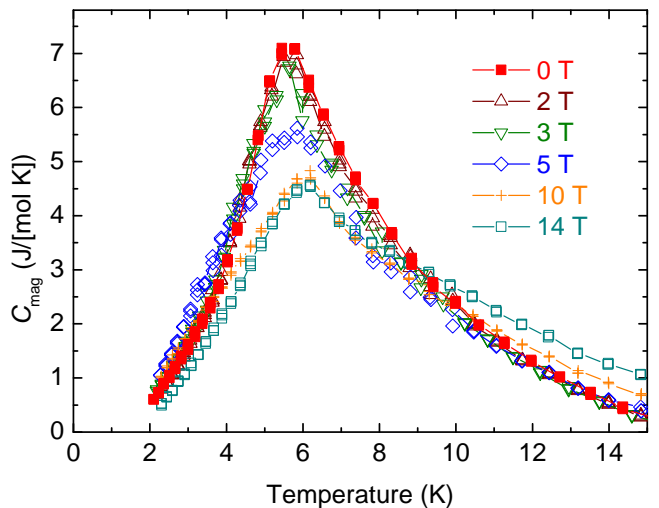


FIG. 3. (Color online) The magnetic contribution to the specific heat, $C_{\text{mag}}(T)$, measured in magnetic fields between 0–14 T.

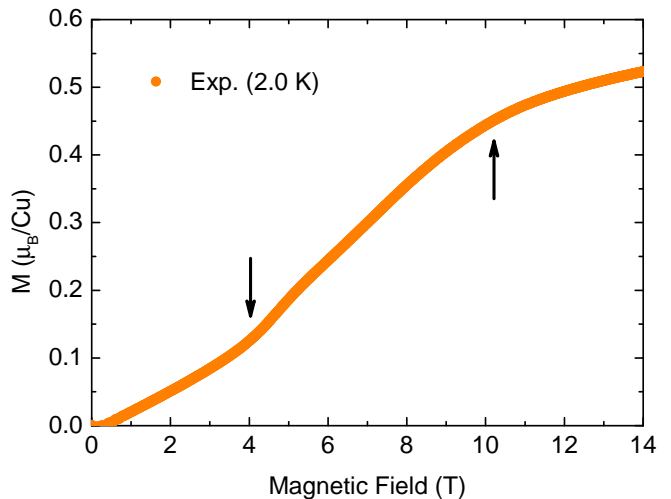


FIG. 4. (Color online) Field-dependent magnetization data $M(H)$ up to 14 T collected at a temperature of 2.0 K. The arrows indicate the kink at about 4 T and the onset of the bending around 10 T. Half saturation is reached at about 12 T.

V. ELECTRONIC STRUCTURE AND MAGNETIC EXCHANGE COUPLINGS

In this section, we derive a microscopic magnetic model that could be used to understand the complex behavior of langite. Microscopic models based on empirical considerations are prone to error because superexchange in Cu^{2+} compounds depends on tiny structural details and cannot be fully captured by empirical rules. Moreover, the presence of four distinct Cu sites in the crystal structure implies that interactions with similar Cu–Cu distances and superexchange pathways are not related by symmetry and may be unequal. Therefore, an empirical

approach for deriving a microscopic magnetic model is bound to fail for langite. Accordingly, we employ numerical electronic structure DFT calculations allowing for a direct computation of individual exchange couplings J_{ij} . In combination with numerical simulations of the thermodynamical properties, such calculations often provided consistent description of the macroscopic magnetic behavior based on microscopic considerations.^{13,23,55,56}

As a first step, LDA calculations were performed, yielding a broad valence band complex of about 10 eV (Fig. 5), which is typical for cuprates.^{40,41,43} Low-energy magnetic excitations should be largely determined by the band complex of eight half-filled bands around the Fermi level, between -0.5 and 0.45 eV. The eight bands arise from the eight Cu^{2+} -ions per unit cell and their corresponding eight half-filled $3d$ -orbitals. Local coordinate systems on the eight Cu-sites (with the local z -axis chosen perpendicular to the CuO_4 -planes and the local x -axis oriented parallel to a Cu–O bond) allow analyzing the orbital character of the half-filled bands. They are essentially of $\text{Cu}(3d_{x^2-y^2})$ and $\text{O}(2p_x, 2p_y)$ character while admixtures from H_2O and particularly SO_4 groups are small. Accordingly, the latter molecules do not play a direct role for the exchange couplings in langite. This set of eight bands is now projected onto Cu-centered Wannier functions (WFs) to evaluate the hopping parameters t_{ij} . Owing to the four different Cu-sites, many different exchange pathways are effective in langite. Table II lists all $|t_{ij}| > 20$ meV as well as the corresponding J_{ij}^{AFM} . The largest interlayer hopping t' is only about -5 meV rendering the spin lattice langite nearly two-dimensional. The positions of the respective exchange pathways in the crystal structure are shown in Fig. 6.

Full exchange constants $J_{ij} = J_{ij}^{\text{FM}} + J_{ij}^{\text{AFM}}$ computed with the LSDA+ U method are provided in the last column of Table II. The two nearest-neighbor (NN) couplings in the type-B chains, J_s and J'_s , are both FM, with J'_s being much smaller than J_s and resulting in ferromagnetic spin chains with alternating exchange couplings. These chains interact antiferromagnetically via J_{II} . This represents the first magnetic sublattice. The difference between J_s and J'_s can be traced back to the relevant Cu–O–Cu angles (Table II). The smaller angle for J_s leads to a stronger FM interaction.

In the edge-sharing type-A chains, J_1 is AFM and about four times stronger than the weak coupling J'_1 . The AFM next-nearest-neighbor (NNN) couplings J_2 and J'_2 are of the same strength as J_1 . The type-A chains may, thus, be described as two-leg ladders (Fig. 6), where J_2 and J'_2 build the legs, while J_1 forms the rungs, and J'_1 is a frustrating diagonal interaction. This represents the second sublattice. The strengths of J_1 and J'_1 can be again traced back to the Cu–O–Cu angles. The smaller bridging angles render J'_1 weaker than J_1 . However, these *antiferromagnetic* couplings are observed for the bridging angles below 100° , while the *ferromagnetic* couplings J_s and J'_s occur for the bridging angles above 100° . This instructive situation highlights limitations of the

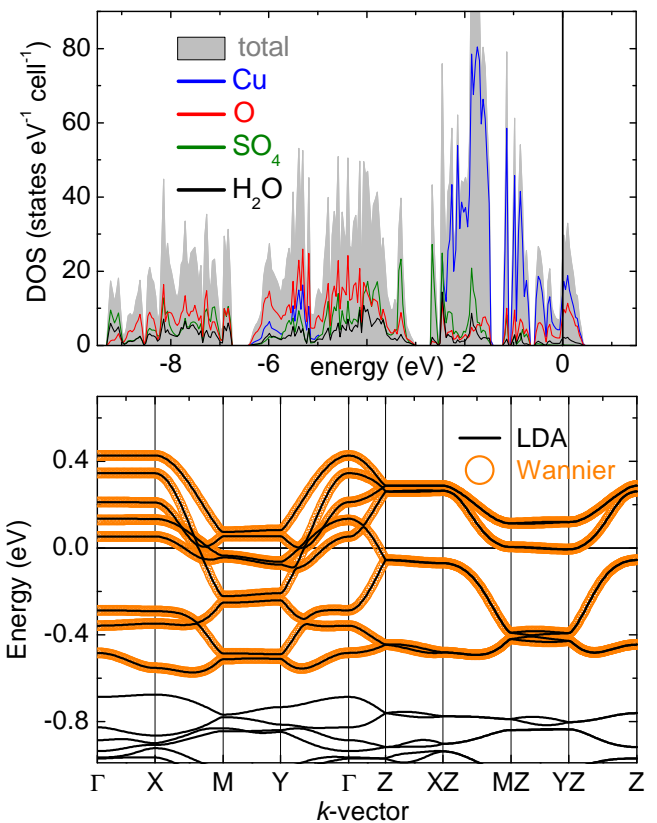


FIG. 5. (Color online) The top panel shows the total and partial density of states (DOS) from LDA calculations. In the lower panel the eight half-filled LDA bands around the Fermi level are shown. "Wannier" denotes bands calculated with Cu-centered Wannier functions.

Goodenough-Kanamori-Anderson rules and the importance of the mutual arrangement of the CuO_4 plaquettes, which share edges (J_1 and J'_1) or corners (J_s and J'_s), respectively.

The two sublattices are coupled to each other by several exchanges, with J_a and J_h being the strongest. The interlayer coupling J' , which is about 0.2 K, may be responsible for the long-range magnetic order observed in langite because three-dimensional order requires the coupling between the layers (Fig. 3). We refrained from estimating J' using LSDA+ U , though, because such small couplings are hard to calculate reliably.⁴³

The exchange couplings given in Table II allow estimating the Curie-Weiss temperature for each Cu-site according to $\theta = S(S+1)/3 \cdot \sum_i (z_i \cdot J_i)$ where S is the electron spin and z_i tells how often a certain coupling J_i occurs on a specific site. Accordingly, we get for the four Cu-sites (Fig. 6): $\theta_1 = -15$ K, $\theta_2 = -3$ K, $\theta_3 = 31$ K, $\theta_4 = 27$ K. The overall Curie-Weiss temperature may be approximated by averaging over all sites yielding $\theta = 10$ K which is in reasonable agreement with the experimental value of 18.2 K (see Sec. IV) regarding the intricate microscopic magnetic model and the large

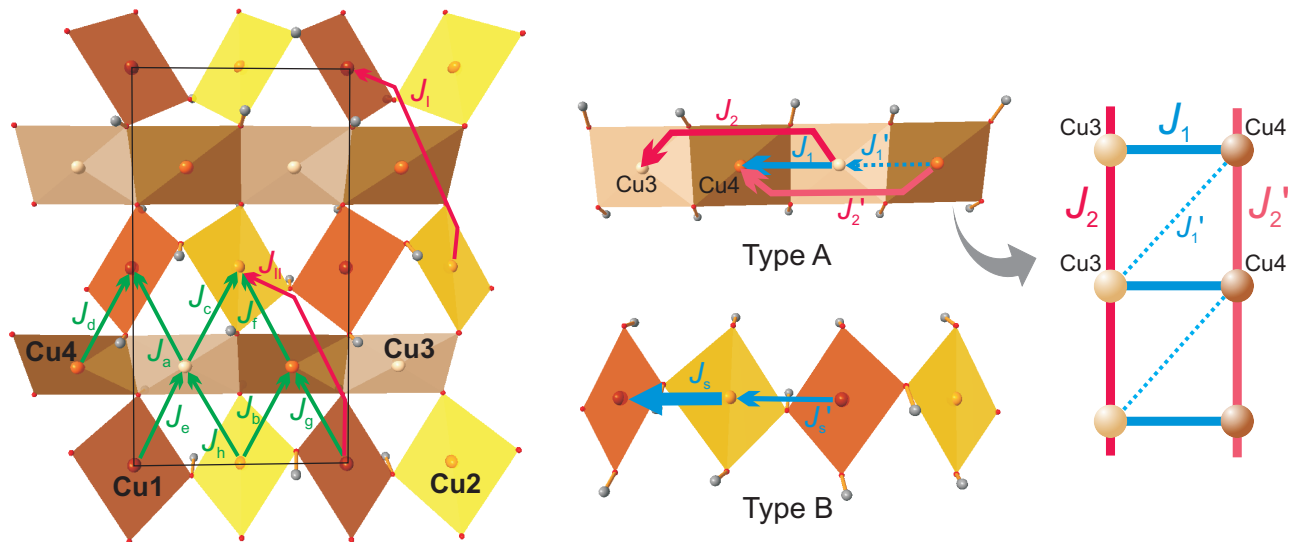


FIG. 6. (Color online) The left panel shows the intralayer exchange pathways. The central panel shows the two chain types and the respective intrachain exchange pathways. A two-leg spin ladder drawn from the intrachain exchange couplings of the typ A chains is shown in the right panel. The antiferromagnetic ladders and the alternating ferromagnetic (type B) chains form the two magnetic sublattices.

number of exchange couplings.

Some of the couplings in Table II show sizable error bars because computational results depend on the exact value of the U_d parameter of LSDA+ U . For example, one can't decide whether J'_1 is ferro- or antiferromagnetic. Therefore, we employed another computational method and calculated exchanges using a HSE06 hybrid DFT-functional,³⁸ as implemented in VASP5.2.³⁹ These calculations were feasible for short-range couplings only. The long-range couplings would require big supercells that cannot be treated with the computationally expensive HSE06 method with the required accuracy. The HSE06 results can be found in the Supplemental Material.⁴⁷

The HSE06 and LSDA+ U results for the short-range couplings are generally similar confirming the FM nature of J_s and J'_s , the AFM nature of J_1 and J'_1 , as well as the $|J_s| > |J'_s|$ and $J'_1 < J_1$ trends discussed above. The couplings between the sublattices are mostly FM.

Disregarding the weak coupling J'_1 , we find that individual magnetic sublattices of langite are non-frustrated because none of the leading couplings J_s , J'_s , and J_{II} for the type-A chains and J_1 , J_2 , and J'_2 for the type-B chains compete to each other. The two leading couplings between the sublattices, FM J_a and AFM J_h , are not frustrated either, because they are compatible with the AFM order between the FM type-B chains, as imposed by J_{II} . However, other inter-sublattice couplings frustrate the spin lattice and render it very complex. Given the large number of non-equivalent exchange couplings and their frustrated nature, we restrict ourselves to a qualitative discussion of the magnetic behavior in Sec. VI below.

VI. DISCUSSION

Magnetic properties of the natural Cu^{2+} -mineral langite are peculiar, yet complicated. Its crystal structure consists of layers formed by directly connected and alternating ordered edge- and corner-sharing chains of CuO_4 plaquettes. Such structural motives can be found in several compounds (see Sec. III) that have same topology of the magnetic layer, but slightly different Cu–O–Cu angles and, thus, potentially different exchange scenarios. Magnetic properties of only one of these materials, brochantite, have been reported. Therefore, it is still an open question which magnetic properties arise when edge- and corner-sharing Cu^{2+} chains are joined into layers, and how these properties are affected by structural details. Our study on langite is intended as a starting point for systematic work on this subject.

As a first step, single crystal XRD-data have been collected down to 100 K and considerable deviations from the earlier crystal structure⁴² have been observed (see Sec. III). The low-temperature crystal structure served then as basis for DFT calculations of the exchange coupling constants since accurate structural data are of crucial importance for a compound like langite with a large number of exchange couplings J_{ij} having similar strength.

The intricate microscopic magnetic model, which we derived from DFT calculations, is quasi-two-dimensional and frustrated. Its direct numerical treatment is hardly possible because quantum Monte-Carlo (QMC) simulations can not be used for a frustrated spin system, while a simplified non-frustrated spin model of two weakly coupled sublattices does not account for all features of the

TABLE II. The transfer integrals t_{ij} (meV) and the AFM contributions to the exchange constants $J_{ij}^{\text{AFM}} = 4t_{ij}^2/U_{\text{eff}}$ (K) where $U_{\text{eff}} = 4.5$ eV. d(Cu–Cu) and Cu–O–Cu denote Cu–Cu distances (Å) and Cu–O–Cu angles (deg), respectively. The J_{ij} (K) given in the last column are calculated with the LSDA+ U method and $U_d = 8.5 \pm 1$ eV and $J_d = 1$ eV.

	d(Cu–Cu)	Cu–O–Cu	t_{ij}	J_{ij}^{AFM}	J_{ij}
type A chains (edge-sharing)					
J'_1	3.011	97.81/98.64	–144	213	9 ± 15
J_1	3.020	99.10/99.49	–155	247	38 ± 20
J'_2	6.030		61	39	36 ± 6
J_2	6.030		59	36	35 ± 6
type B chains (corner-sharing)					
J_s	2.983	101.05	40	16	-74 ± 10
J'_s	3.049	104.706	62	40	-23 ± 3
J_{s2}	6.030		31	10	< 1
J'_{s2}	6.030		30	9	< 1
nearest-neighbor interchain couplings					
J_a	3.139	103.55	85	74	-19 ± 1
J_b	3.144	105.08	–109	123	5 ± 5
J_c	3.163	106.64	91	85	-6 ± 2
J_d	3.168	105.23	109	121	8 ± 5
J_e	3.186	106.65	–91	85	0 ± 4
J_f	3.190	106.61	94	91	-12 ± 2
J_g	3.219	106.10	–92	87	-13 ± 1
J_h	3.229	109.23	–107	119	31 ± 7
next-nearest-neighbor interchain couplings					
J_I	6.309		–51	27	10 ± 10
J_{II}	6.407		–61	38	51 ± 20
interlayer coupling					
J'	7.874		–5	0.2	

experimental data. The ground state of a frustrated spin system in 2D could be accessed by using the density-matrix renormalization group (DMRG) technique that, however, can not be applied at finite temperatures, where thermodynamic properties have been measured experimentally.

Experimental magnetization curve of langite, where half-saturation is reached around 12 T, shows that a fraction of the Cu^{2+} spins in langite is coupled ferromagnetically. This observation can be paralleled to the predominantly ferromagnetic couplings within the type-B chains that should saturate as soon as magnetic field overcomes the effect of the AFM coupling J_{II} . There is only one J_{II} coupling per Cu site, so the half-saturation should be reached at $H_{s1} = k_B J_{II}/(g\mu_B) \simeq 38$ T, which is much higher than 12 T observed experimentally. The origin of this discrepancy is not entirely clear. The presence of the second sublattice (type-A chains) and the frustrated interactions between the sublattices may overcome the effect of J_{II} and facilitate the saturation of the type-B sublattice already in low field, although de-

tailed investigation of this behavior requires numerical simulations for the full spin lattice of langite, which are not feasible, as we explained above. The type-A sublattice is antiferromagnetic. Its saturation is expected at $H_{s2} = k_B/(g\mu_B)(J_1 + J_2 + J'_2) \simeq 81$ T and would be interesting to probe experimentally.

Magnetic susceptibility of langite lacks a broad maximum that would be expected in a quasi-2D antiferromagnet. This observation is also consistent with the presence of the mostly FM sublattice of the type-B chains that lack any susceptibility maximum and, thus, mask the susceptibility maximum related to the type-A chains, which are AFM. A similar behavior has been observed in CuP_2O_6 ,²³ where none of the sublattices is ferromagnetic, but very weak couplings in one of the sublattices render half of the spins paramagnetic down to low temperatures, and no susceptibility maximum is observed down to T_N .

The temperature of the antiferromagnetic ordering in langite, $T_N \simeq 5.7$ K, is quite low compared to leading exchange couplings $|J_s|$, J_I , J_{II} , J_2 , and J'_2 that are at least 35 – 40 K each. We tentatively find $T_N/\bar{J} < 0.2$, which is very low for a quasi-2D antiferromagnet,⁵⁷ although a correct definition of an effective intralayer coupling \bar{J} may be difficult in this case given the very complex nature of the spin lattice. We note also that the spin lattice of langite is nearly 2D, because the interlayer coupling J' is less than 1% of the leading intralayer couplings, so the effect of two-dimensionality may be important for the stability of the long-range-ordered magnetic state.

Altogether, we are able to explain main features of the magnetic behavior of langite qualitatively in terms of the two sublattices, the type-B chains with mostly FM couplings and the type-A chains with only AFM couplings. More subtle features, such as the bends of the magnetization curve around 4 T, require further investigation and may be related to effects of magnetic anisotropy that lie beyond the scope of our study.

Let us now compare langite to Cu^{2+} minerals with similar structural features. In antlerite $\text{Cu}_3(\text{OH})_4\text{SO}_4$,^{24,58} two side chains of the B-type encompass the central chain of the A-type that together form a ribbon, which is sometimes considered as a three-leg spin ladder. Neutron scattering revealed ordered magnetic moment of $0.88 \mu_B$ on the terminal (type-B) chains and zero magnetic moment on the central (type-A) chains.²⁴ A similar type of magnetic order is expected in langite, where spins in the type-B chains will form long-range magnetic order, whereas spins in the type-A chains should develop gapped ground state with zero ordered moment, as typical for two-leg spin ladders. A direct study of the magnetic ground state of langite would be, thus, very interesting and may reveal generic features of the edge-sharing (type-A) and corner-sharing (type-B) chains in Cu^{2+} oxide materials.

Another Cu^{2+} mineral, brochantite $\text{Cu}_4(\text{OH})_6\text{SO}_4$, is remarkably different from both langite and antlerite. From the chemistry perspective, it is a dehydrated version of langite featuring same type of magnetic layers.

However, details of their geometry are somewhat different because water molecules are missing, and the separation between the layers is about twice shorter than in langite. Neutron diffraction reports very small magnetic moments within the corner-sharing type-B chains ($0.22 \mu_B$) and much larger ordered moments within the type-A chains ($0.74 \mu_B$).²⁹ This is very different from antlerite and may indicate a different exchange topology. Indeed, the Curie-Weiss temperature of brochantite ($\theta \simeq 90 \text{ K}$)²⁹ is much higher than 18 K and 4 K in langite and antlerite,⁵⁹ respectively. Moreover, brochantite features a broad susceptibility maximum around 60 K, far above T_N , while neither langite nor antlerite show such broad maxima. These features suggest that magnetic interactions in brochantite are predominantly AFM, whereas langite and antlerite reveal a subtle interplay of FM and AFM exchange couplings. Further microscopic insight into these differences is clearly needed and requires a systematic computational study of the aforementioned Cu^{2+} minerals.

Naively, the AFM nature of brochantite can be ascribed to the larger Cu–O–Cu angles in the range $105.6 - 122.5^\circ$, while the Cu–O–Cu angles in langite are, generally, smaller ($103.5 - 109.2^\circ$). However, this simple analysis in the spirit of Goodenough-Kanamori-Anderson rules may often be misleading. We have mentioned that the values of the Cu–O–Cu bridging angles account for $|J_s| > |J_s'|$ and $J_1 > J_1'$, but they do not explain why J_s and J_s' are FM, while J_1 and J_1' with the smaller bridging angles are AFM. Other effects may be important in this case. In particular, hydrogen atoms bonding to the bridging oxygen have strong influence on the superexchange.⁴¹ Hydrogen atoms located out of the CuO_4 planes favor FM exchange, which may be relevant to J_s and J_s' in langite. The twisting of the CuO_4 plaquettes may also be important. The plaquettes in the type-A chains are almost coplanar that should be favorable for electron hoppings and AFM superexchange. By contrast, the strong twisting of the neighboring plaquettes in the type-B chains yields FM couplings.

VII. SUMMARY

In summary, structural and magnetic properties of the Cu^{2+} mineral langite have been investigated in a joint experimental and theoretical study. Crystal structure of langite was refined in the 100 – 280 K temperature range using single-crystal XRD, and the H-positions were subsequently determined for the 100 K structure using theoretical DFT-approach. The crystal structure consists of two types of directly connected Cu-chains, edge- and corner-sharing, which form layers separated from each other by about 7.5 \AA . These layers are a common structural motive in cuprate minerals but, so far, have been scarcely investigated with respect to their magnetic properties. Along with the fact that both chain-types taken on their own have revealed fascinating magnetic proper-

ties, it intrigued us what kind of physics may arise from their combination into layers.

Experimentally, langite reveals subtle balance between the ferro- and antiferromagnetic exchange couplings, as reflected in its relatively low antiferromagnetic Curie-Weiss temperature $\theta \simeq 18 \text{ K}$. No broad maximum in the magnetic susceptibility has been observed. The susceptibility keeps increasing down to $T_N \simeq 5.7 \text{ K}$, where a broad λ -type anomaly occurs in the specific heat. Magnetization as a function of external field reaches half-saturation around 12 T and reveals several bends in lower fields.

These observations indicate that part of the Cu^{2+} spins in langite are coupled ferromagnetically or weakly antiferromagnetically. These spins saturate around 12 T and mask the broad maximum of the magnetic susceptibility that would be otherwise observed in a quasi-two dimensional quantum magnet. Basic features of the magnetic behavior are rationalized on the microscopic level, where predominantly ferromagnetic couplings are found in corner-sharing structural chains, whereas edge-sharing chains are antiferromagnetic. The couplings between these chains are at least partially frustrated, and a quantitative modelling of the magnetic behavior turns out to be quite challenging considering the large number of nonequivalent exchange couplings and magnetic frustration in 2D. Weak interlayer couplings below 0.2 K confirm that the spin lattice of langite is quasi-2D.

Langite bears many similarities to antlerite, where both corner- and edge-sharing chains are found too, although they form three-leg strips instead of infinite layers. Our microscopic analysis suggests that only half of the Cu^{2+} spins may be ordered in langite below T_N , because the Cu^{2+} ions in edge-sharing chains form a spin ladder having the gapped singlet ground state. This prediction extends the similarity to antlerite, where “idle” spins with zero ordered moment were found in the edge-sharing chain experimentally. Further investigation of langite with neutron scattering would be very interesting and will improve our understanding of complex quantum magnets, where sublattices with different topology and interactions coexist.

ACKNOWLEDGMENTS

We acknowledge the experimental support by Yurii Prots and Horst Borrmann (laboratory XRD). We would also like to thank Prof. Klaus Thalheim and the Senckenberg Naturhistorische Sammlung Dresden for providing the langite sample from Slovakia (inventory number 18940 Sy). AT and OJ were supported by the Mobilitas program of the ESF (grant numbers MTT77 and MJD447). AT also acknowledges financial support by the Alexander von Humboldt Foundation and Federal Ministry for Education and Research through the Sofja Kovalevskaya Award.

- * st.lebernegg@gmail.com
- † Helge.Rosner@cpfs.mpg.de
- ¹ M. Hase, I. Terasaki, and K. Uchinokura, *Phys. Rev. Lett.* **70**, 3651 (1993).
 - ² S. Seki, X. Z. Yu, S. Ishiwata, and Y. Tokura, *Science* **13**, 198 (2012).
 - ³ T. Giamarchi, C. Rüegg, and O. Tchernyshyov, *Nat. Phys.* **4**, 198 (2008).
 - ⁴ J. Schlappa, K. Wohlfeld, K. J. Zhou, M. Mourigal, M. W. Haverkort, V. N. Strocov, L. Hozoi, C. Monney, S. Nishimoto, S. Singh, A. Revcolevschi, J.-S. Caux, L. Patthey, H. M. Ronnow, J. van den Brink, and T. Schmitt, *Nature* **485**, 82 (2012).
 - ⁵ H. Rosner, H. Eschrig, R. Hayn, S.-L. Drechsler, and J. Málek, *Phys. Rev. B* **56**, 3402 (1997).
 - ⁶ A. Möller, M. Schmitt, W. Schnelle, T. Förster, and H. Rosner, *Phys. Rev. B* **80**, 125106 (2009).
 - ⁷ K. Nawa, T. Yajima, Y. Okamoto, and Z. Hiroi, *Inorg. Chem* **54**, 5566 (2015).
 - ⁸ T. Masuda, A. Zheludev, A. Bush, M. Markina, and A. Vasiliev, *Phys. Rev. Lett.* **92**, 177201 (2004).
 - ⁹ L. Capogna, M. Reehuis, A. Maljuk, R. K. Kremer, B. Ouladdiaf, M. Jansen, and B. Keimer, *Phys. Rev. B* **82**, 014407 (2010).
 - ¹⁰ F. Sapiña, J. R. guez Carvajal, M. J. Sanchis, R. I. nez, A. Beltrán, and D. Beltrán, *Solid State Comm.* **74**, 779 (1990).
 - ¹¹ K. Caslin, R. K. Kremer, F. S. Razavi, A. Schulz, A. Muñoz, F. Pertlik, J. Liu, M.-H. Whangbo, and J. M. Law, *Phys. Rev. B* **89**, 014412 (2014).
 - ¹² M. G. Banks, R. K. Kremer, C. Hoch, A. Simon, B. Ouladdiaf, J.-M. Broto, H. Rakoto, C. Lee, and M.-H. Whangbo, *Phys. Rev. B* **80**, 024404 (2009).
 - ¹³ C. Lee, J. Liu, M.-H. Whangbo, H.-J. Koo, R. K. Kremer, and A. Simon, *Phys. Rev. B* **86**, 060407 (2012).
 - ¹⁴ B. Willenberg, M. Schäpers, K. C. Rule, S. Süllow, M. Reehuis, H. Ryll, B. Klemke, K. Kiefer, W. Schottenhamel, B. Büchner, B. Ouladdiaf, M. Uhlarz, R. Beyer, J. Wosnitza, and A. U. B. Wolter, *Phys. Rev. Lett.* **108**, 117202 (2012).
 - ¹⁵ S. Seki, Y. Yamasaki, M. Soda, M. Matsuura, K. Hirota, and Y. Tokura, *Phys. Rev. Lett.* **100**, 127201 (2008).
 - ¹⁶ Y. Yasui, K. Sato, Y. Kobayashi, and M. Sato, *J. Phys. Soc. Jpn.* **78**, 084720 (2009); Y. Kobayashi, K. Sato, Y. Yasui, T. Moyoshi, M. Sato, and K. Kakurai, *ibid.* **78**, 084721 (2009).
 - ¹⁷ Y. Yasui, M. Sato, and I. Terasaki, *J. Phys. Soc. Jpn.* **80**, 033707 (2011).
 - ¹⁸ F. C. Chou, A. Aharony, R. J. Birgeneau, O. Entin-Wohlman, M. Greven, A. B. Harris, M. A. Kastner, Y. J. Kim, D. S. Kleinberg, Y. S. Lee, and Q. Zhu, *Phys. Rev. Lett.* **78**, 535 (1997).
 - ¹⁹ Y. J. Kim, A. Aharony, R. J. Birgeneau, F. C. Chou, O. Entin-Wohlman, R. W. Erwin, M. Greven, A. B. Harris, M. A. Kastner, I. Y. Korenblit, Y. S. Lee, and G. Shirane, *Phys. Rev. Lett.* **83**, 852 (1999).
 - ²⁰ M. A. Kastner, A. Aharony, R. J. Birgeneau, F. C. Chou, O. Entin-Wohlman, M. Greven, A. B. Harris, Y. J. Kim, Y. S. Lee, M. E. Parks, and Q. Zhu, *Phys. Rev. B* **59**, 14702 (1999).
 - ²¹ Y. J. Kim, R. J. Birgeneau, F. C. Chou, M. Greven, M. A. Kastner, Y. S. Lee, B. O. Wells, A. Aharony, O. Entin-Wohlman, I. Y. Korenblit, A. B. Harris, R. W. Erwin, and G. Shirane, *Phys. Rev. B* **64**, 024435 (2001).
 - ²² A. B. Harris, A. Aharony, O. Entin-Wohlman, I. Y. Korenblit, R. J. Birgeneau, and Y.-J. Kim, *Phys. Rev. B* **64**, 024436 (2001).
 - ²³ R. Nath, K. M. Ranjith, J. Sichelschmidt, M. Baenitz, Y. Skourski, F. Alet, I. Rousochatzakis, and A. A. Tsirlin, *Phys. Rev. B* **89**, 014407 (2014).
 - ²⁴ S. Vilminot, M. Richard-Plouet, G. André, D. Swierczynski, M. Guillot, F. Boureé-Vignerone, and M. Drillon, *J. Sol. Stat. Chem.* **170**, 255 (2003).
 - ²⁵ S. Lebernegg, A. A. Tsirlin, O. Janson, I. Rousochatzakis, and H. Rosner, unpublished.
 - ²⁶ D. Y. Pushcharovsky, R. K. Rastsvetaeva, and H. Sarp, *J. Alloy. Compd.* **239**, 23 (1996).
 - ²⁷ D. Ginderow and F. Cesbron, *Acta Cryst. C* **39**, 1605 (1983).
 - ²⁸ G. Giester, B. Rieck, and F. Brandstaetter, *Miner. Petrol.* **63**, 19 (1998).
 - ²⁹ S. Vilminot, M. Richard-Plouet, G. Andre, D. Swierczynski, F. Bouree-Vignerone, and M. Kurmoo, *Dalton Trans.*, 1455 (2006).
 - ³⁰ M. R. Bissengaliyeva, N. S. Bekturganov, D. B. Gogol, S. T. Taimassova, T. A. Koketai, and M. A. Bespyatov, *J. Chem. Eng. Data* **58**, 2904 (2013).
 - ³¹ G. M. Sheldrick, *Acta Cryst. A* **64**, 112 (2008).
 - ³² L. J. Farrugia, *J. Appl. Cryst.* **45**, 849 (2012).
 - ³³ K. Koepernik and H. Eschrig, *Phys. Rev. B* **59**, 1743 (1999).
 - ³⁴ J. P. Perdew and Y. Wang, *Phys. Rev. B* **45**, 13244 (1992).
 - ³⁵ J. P. Perdew, K. Burke, and M. Ernzerhof, *Phys. Rev. Lett.* **77**, 3865 (1996).
 - ³⁶ V. I. Anisimov, J. Zaanen, and O. K. Andersen, *Phys. Rev. B* **44**, 943 (1991).
 - ³⁷ V. I. Anisimov, F. Aryasetiawan, and A. I. Lichtenstein, *J. Phys.: Condens. Matter* **9**, 767 (1997).
 - ³⁸ J. Heyd, G. E. Scuseria, and M. Ernzerhof, *J. Chem. Phys.* **118**, 8207 (2003); O. A. Vydrov, J. Heyd, A. V. Krukau, and G. E. Scuseria, *J. Chem. Phys.* **125**, 074106 (2006).
 - ³⁹ G. Kresse and J. Furthmüller, *Comput. Mater. Sci.* **6**, 15 (1996); *Phys. Rev. B* **54**, 11169 (1996).
 - ⁴⁰ S. Lebernegg, A. A. Tsirlin, O. Janson, and H. Rosner, *Phys. Rev. B* **88**, 224406 (2013).
 - ⁴¹ S. Lebernegg, A. A. Tsirlin, O. Janson, and H. Rosner, *Phys. Rev. B* **87**, 235117 (2013).
 - ⁴² M. Gentsch and K. Weber, *Acta Cryst. C* **40**, 1309 (1984).
 - ⁴³ S. Lebernegg, A. A. Tsirlin, O. Janson, and H. Rosner, *Phys. Rev. B* **89**, 165127 (2014).
 - ⁴⁴ S. Lebernegg, M. Schmitt, A. A. Tsirlin, O. Janson, and H. Rosner, *Phys. Rev. B* **87**, 155111 (2013).
 - ⁴⁵ H. Jeschke, I. Opahle, H. Kandpal, R. Valentí, H. Das, T. Saha-Dasgupta, O. Janson, H. Rosner, A. Brühl, B. Wolf, M. Lang, J. Richter, S. Hu, X. Wang, R. Peters, T. Pruschke, and A. Honecker, *Phys. Rev. Lett.* **106**, 217201 (2011).
 - ⁴⁶ H. J. Xiang, E. J. Kan, S.-H. Wei, M.-H. Whangbo, and X. G. Gong, *Phys. Rev. B* **84**, 224429 (2011).
 - ⁴⁷ See Supplementary Material for single-crystal crystallographic data collected at temperatures between 100–280 K,

the back ground contributions to $C_p(T)$ at $H=0$ T, powder XRD pattern of Langite and exchange constants J_{ij} from HSE06 hybrid DFT-calculations, description of the tetramer model provided as an alternative to the model of two magnetic sublattices.

- ⁴⁸ M. Braden, G. Wilkendorf, J. Lorenzana, M. Aïn, G. J. McIntyre, M. Behruzi, G. Heger, G. Dhahlenne, and A. Revcolevschi, *Phys. Rev. B* **54**, 1105 (1996).
- ⁴⁹ A. A. Tsirlin, O. Janson, S. Lebernegg, and H. Rosner, *Phys. Rev. B* **87**, 064404 (2013).
- ⁵⁰ A. Yogi, N. Ahmed, R. Nath, A. A. Tsirlin, S. Kundu, A. V. Mahajan, J. Sichelschmidt, B. Roy, and Y. Furukawa, *Phys. Rev. B* **91**, 024413 (2015).
- ⁵¹ N. Ahmed, A. A. Tsirlin, and R. Nath, *Phys. Rev. B* **91**, 214413 (2015).
- ⁵² R. Nath, K. M. Ranjith, B. Roy, D. C. Johnston, Y. Furukawa, and A. A. Tsirlin, *Phys. Rev. B* **90**, 024431 (2014).
- ⁵³ D. C. Johnston, R. K. Kremer, M. Troyer, X. Wang, A. Klümper, S. L. Bud'ko, A. F. Panchula, and P. C. Canfield, *Phys. Rev. B* **61**, 9558 (2000).
- ⁵⁴ For example: Y. C. Arango, E. Vavilova, M. Abdel-Hafiez, O. Janson, A. A. Tsirlin, H. Rosner, S.-L. Drechsler, M. Weil, G. Nénert, R. Klingeler, O. Volkova, A. Vasiliev, V. Kataev, and B. Büchner, *Phys. Rev. B* **84**, 134430 (2011).
- ⁵⁵ M. Schmitt, O. Janson, M. Schmidt, S. Hoffmann, W. Schnelle, S.-L. Drechsler, and H. Rosner, *Phys. Rev. B* **79**, 245119 (2009).
- ⁵⁶ S. Lebernegg, A. A. Tsirlin, O. Janson, R. Nath, J. Sichelschmidt, Y. Skourski, G. Amthauer, and H. Rosner, *Phys. Rev. B* **84**, 174436 (2011).
- ⁵⁷ C. Yasuda, S. Todo, K. Hukushima, F. Alet, M. Keller, M. Troyer, and H. Takayama, *Phys. Rev. Lett.* **94**, 217201 (2005).
- ⁵⁸ H.-J. Koo, R. K. Kremer, and M.-H. Whangbo, *J. Phys. Soc. Jpn.* **81**, 063704 (2012).
- ⁵⁹ S. Hara, H. Kondo, and H. Sato, *J. Phys. Soc. Jpn.* **80**, 043701 (2011).

Supporting Material

TABLE III. Obtained lattice parameters of Langite, details of the refinement procedure and settings for the single-crystal XRD at various temperatures.

T (K)	280	250	220	140	100
Crystallographic data					
S.G.	<i>Pc</i>	<i>Pc</i>	<i>Pc</i>	<i>Pc</i>	<i>Pc</i>
<i>a</i> (Å)	7.1412(8)	7.1370(8)	7.1349(8)	7.1255(8)	7.1231(8)
<i>b</i> (Å)	6.0468(7)	6.0427(7)	6.0400(7)	6.0312(7)	6.0305(7)
<i>c</i> (Å)	11.2328(12)	11.2238(12)	11.2204(12)	11.1996(12)	11.1935(12)
β (deg)	90.0716	90.0743(14)	90.0892(14)	90.1279(14)	90.1479814
Volume(Å ³)	485.048	484.05(9)	483.54(9)	481.31(9)	480.83(9)
Z	2	2	2	2	2
Dx (mg/m ³)	3.274	3.281	3.285	3.300	3.303
Absorption (cm ⁻¹)	8.924	8.942	8.951	8.993	9.002
Radiation	Mo(K α)				
Data collection					
Theta range (deg)	2.85–29.00	2.85–29.01	2.86–28.87	2.86–28.97	2.86–28.97
Reflection collected	5811	5773	5764	5726	5657
Independent reflections	2366	2358	2359	2355	2334
Completeness of data	99.8	99.8	99.8	99.8	99.8
R_{int} (%)	1.94	1.95	2.62	4.1	5.2
R_1 ($I > 2\sigma(I)$)	3.28	3.46	3.85	5.2	4.64
wR_2	6.33	6.84	7.39	8.01	6.77
Largest diff. peak/hole (e \times Å ³)	0.53/-0.75	0.99/-0.86	1.12/-0.63	0.97/-0.90	1.16/-0.88

TABLE IV. Refined atomic positions (in fractions of lattice parameters) and isotropic atomic displacement parameters U_{iso} ($\times 10^{-2}$ Å²) of Langite collected at 140 K. All atoms are in the general position $2a$ of the space group $P1c1$. OW denotes O of the H₂O molecules. OS atoms belong to the SO₄ tetrahedra.

Atom	x/a	y/b	z/c	U_{iso}
Cu1	0.99970(15)	0.9975(2)	0.49967(11)	0.61(3)
Cu2	0.99299(15)	0.4927(2)	0.50197(10)	0.55(3)
Cu3	1.00363(16)	0.7559(2)	0.75290(12)	0.53(2)
Cu4	1.00899(16)	0.25469(18)	0.75168(12)	0.47(2)
S	0.5775(5)	0.1846(4)	0.4204(3)	0.82(4)
O1	0.8870(10)	0.9993(11)	0.6637(7)	0.68(14)
O2	0.8874(10)	0.5052(11)	0.6661(7)	0.50(14)
O3	1.1155(10)	0.5094(11)	0.8439(7)	0.59(15)
O4	1.1402(9)	0.2462(12)	0.5597(7)	0.48(14)
O5	0.8583(9)	0.7436(10)	0.4428(6)	0.63(14)
O6	1.1253(9)	1.0059(11)	0.8407(7)	0.40(15)
OS1	0.7837(9)	0.2316(10)	0.4119(6)	0.61(13)
OS2	0.5374(9)	0.0648(11)	0.5333(7)	1.38(15)
OS3	1.4760(10)	0.4033(11)	0.4229(7)	1.27(15)
OS4	1.5146(10)	0.9525(11)	0.8181(7)	1.55(15)
OW1	1.2595(10)	0.7411(11)	0.6016(8)	0.94(15)
OW2	0.5157(11)	0.4272(13)	0.6982(8)	1.60(17)

TABLE V. Refined atomic positions (in fractions of lattice parameters) and isotropic atomic displacement parameters U_{iso} ($\times 10^{-2} \text{ \AA}^2$) of Langite collected at 220 K. All atoms are in the general position $2a$ of the space group $P1c1$. OW denotes O and H atoms of the H_2O molecules. OS atoms belong to the SO_4 tetrahedra.

Atom	x/a	y/b	z/c	U_{iso}
Cu1	0.99948(9)	0.99780(11)	0.49992(6)	0.926(18)
Cu2	0.99321(9)	0.49226(12)	0.50203(6)	0.897(19)
Cu3	1.00292(10)	0.75525(12)	0.75311(7)	0.892(15)
Cu4	1.00889(10)	0.25436(11)	0.75165(7)	0.830(17)
S	0.5780(3)	0.1835(2)	0.4194(2)	1.15(3)
O1	0.8890(7)	0.9981(6)	0.6620(5)	0.97(9)
O2	0.8896(7)	0.5053(6)	0.6646(4)	0.88(9)
O3	1.1182(7)	0.5106(6)	0.8425(5)	0.92(10)
O4	1.1406(6)	0.2465(7)	0.5599(4)	0.85(10)
O5	0.8597(7)	0.7453(6)	0.4432(4)	0.98(10)
O6	1.1249(6)	1.0072(6)	0.8388(4)	0.69(10)
OS1	0.7825(7)	0.2318(6)	0.4116(4)	1.13(9)
OS2	0.5400(6)	0.0616(8)	0.5320(5)	2.49(11)
OS3	1.4768(6)	0.3973(7)	0.4229(4)	1.96(10)
OS4	1.5172(7)	0.9495(8)	0.8164(5)	2.44(11)
OW1	1.2635(7)	0.7403(7)	0.6001(5)	1.82(10)
OW2	0.5190(8)	0.4213(8)	0.6976(5)	2.61(11)

TABLE VI. Refined atomic positions (in fractions of lattice parameters) and isotropic atomic displacement parameters U_{iso} ($\times 10^{-2} \text{ \AA}^2$) of Langite collected at 250 K. All atoms are in the general position $2a$ of the space group $P1c1$. OW denotes O and H atoms of the H_2O molecules. OS atoms belong to the SO_4 tetrahedra.

Atom	x/a	y/b	z/c	U_{iso}
Cu1	0.99955(8)	0.99755(10)	0.49986(6)	0.944(16)
Cu2	0.99336(8)	0.49193(10)	0.50201(5)	0.878(17)
Cu3	1.00281(9)	0.75523(11)	0.75317(6)	0.897(14)
Cu4	1.00877(9)	0.25437(9)	0.75180(6)	0.805(15)
S	0.5780(3)	0.1835(2)	0.4193(2)	1.24(2)
O1	0.8878(6)	0.9990(5)	0.6620(4)	0.78(8)
O2	0.8886(6)	0.5053(5)	0.6637(4)	0.85(8)
O3	1.1165(6)	0.5096(6)	0.8416(4)	0.96(9)
O4	1.1403(6)	0.2455(6)	0.5596(4)	0.87(8)
O5	0.8608(6)	0.7446(5)	0.4427(4)	0.83(8)
O6	1.1250(6)	1.0060(5)	0.8381(4)	0.78(9)
OS1	0.7835(6)	0.2322(5)	0.4113(4)	1.00(8)
OS2	0.5399(6)	0.0620(7)	0.5316(4)	2.51(9)
OS3	1.4780(6)	0.3970(6)	0.4231(4)	2.08(9)
OS4	1.5165(6)	0.9503(7)	0.8158(4)	2.49(10)
OW1	1.2626(6)	0.7402(6)	0.6006(4)	1.72(9)
OW2	0.5193(7)	0.4239(8)	0.6992(5)	2.65(10)

TABLE VII. Refined atomic positions (in fractions of lattice parameters) and isotropic atomic displacement parameters U_{iso} ($\times 10^{-2} \text{ \AA}^2$) of Langite collected at 280 K. All atoms are in the general position $2a$ of the space group $P1c1$. OW denotes O and H atoms of the H_2O molecules. OS atoms belong to the SO_4 tetrahedra.

Atom	x/a	y/b	z/c	U_{iso}
Cu1	0.9997(1)	0.9976(1)	0.4999(0)	0.983(14)
Cu2	0.9932(1)	0.4919(1)	0.5019(0)	0.968(15)
Cu3	1.0028(1)	0.7552(1)	0.7531(1)	0.938(12)
Cu4	1.0090(1)	0.2541(1)	0.7517(1)	0.874(14)
S	0.5778(3)	0.1832(2)	0.4193(2)	1.35(2)
O1	0.8878(5)	0.9988(4)	0.6631(4)	0.99(7)
O2	0.8882(5)	0.5036(5)	0.6648(4)	0.92(7)
O3	1.1168(5)	0.5096(5)	0.8427(4)	0.94(8)
O4	1.1407(5)	0.2452(5)	0.5600(4)	1.01(8)
O5	0.8608(5)	0.7446(4)	0.4433(3)	0.91(7)
O6	1.1243(5)	1.0060(5)	0.8392(4)	0.99(8)
OS1	0.7832(5)	0.2308(5)	0.4109(3)	1.17(7)
OS2	0.5399(5)	0.0618(6)	0.5312(4)	2.63(8)
OS3	1.4770(5)	0.3950(6)	0.4232(4)	2.36(8)
OS4	1.5171(6)	0.9498(6)	0.8156(4)	2.64(9)
OW1	1.2620(6)	0.7399(6)	0.6010(4)	2.03(9)
OW2	0.5177(6)	0.4177(7)	0.7000(5)	3.12(10)

TABLE VIII. Selected bond lengths (\AA) for the crystal structures of Langite collected at different temperatures.

T (K)		280	250	220	140	100
Cu1	O4	1.927(3)	1.925(4)	1.923(4)	1.924(7)	1.924(7)
	O6	1.931(3)	1.931(4)	1.930(4)	1.940(6)	1.938(6)
	O1	2.000(4)	1.987(5)	1.982(6)	2.007(8)	2.003(7)
	O7	2.013(4)	2.024(5)	2.017(5)	1.995(8)	2.006(7)
	O8	2.319(3)	2.319(4)	2.319(4)	2.307(6)	2.302(6)
Cu2	O6	1.914(3)	1.916(4)	1.918(4)	1.910(6)	1.913(6)
	O4	1.939(3)	1.933(4)	1.932(4)	1.930(7)	1.940(6)
	O2	1.979(4)	1.964(5)	1.970(4)	1.989(7)	1.977(7)
	O3	1.995(4)	2.004(5)	2.000(6)	1.976(8)	1.983(8)
	O8	2.406(3)	2.397(4)	2.401(4)	2.391(6)	2.385(6)
Cu3	O1	1.966(3)	1.973(4)	1.964(4)	1.960(7)	1.970(6)
	O3	1.970(3)	1.961(4)	1.966(5)	1.970(7)	1.961(7)
	O2	1.992(3)	1.988(4)	1.980(4)	1.978(7)	1.984(6)
	O7	1.997(3)	1.991(4)	1.999(4)	1.997(7)	1.990(7)
	O8	2.368(4)	2.368(5)	2.375(5)	2.376(7)	2.370(6)
Cu4	O7	1.974(4)	1.969(4)	1.967(4)	1.982(7)	1.980(7)
	O2	1.993(4)	2.003(4)	1.994(4)	1.987(7)	1.984(6)
	O3	2.006(4)	1.996(4)	2.011(5)	2.000(7)	1.996(7)
	O1	2.031(3)	2.035(4)	2.035(5)	2.024(7)	2.025(6)
	O4	2.351(4)	2.353(4)	2.348(5)	2.347(8)	2.344(7)
	O6	2.398(4)	2.389(5)	2.398(5)	2.397(7)	2.372(7)
S1	O11	1.470(4)	1.475(4)	1.480(5)	1.506(7)	1.488(63)
	O12	1.480(5)	1.482(5)	1.473(5)	1.482(8)	1.491(7)
	O10	1.481(5)	1.484(5)	1.487(6)	1.485(8)	1.493(7)
	O8	1.498(4)	1.499(5)	1.491(5)	1.500(7)	1.501(6)

TABLE IX. The total nearest-neighbor J_{ij} (K) calculated with the HSE06 hybrid functional as implemented in VASP5.2 in comparison with the results from LSDA+ U calculations using the `fplo9.07-41` code, $U_d = 8.5 \pm 1$ eV and $J_d = 1$ eV. $d(\text{Cu-Cu})$ and Cu-O-Cu denote Cu-Cu distances (\AA) and Cu-O-Cu angles (deg), respectively.

	$d(\text{Cu-Cu})$	Cu-O-Cu	HSE06	LSDA+ U
J_s	2.983	101.05	-116	-74 ± 10
J'_1	3.011	97.81/98.64	21	9 ± 15
J_1	3.020	99.10/99.49	58	38 ± 20
J'_s	3.049	104.706	-65	-23 ± 3
J_a	3.139	103.55	-52	-19 ± 1
J_b	3.144	105.08	-23	5 ± 5
J_c	3.163	106.64	-43	-6 ± 2
J_d	3.168	105.23	-16	8 ± 5
J_e	3.186	106.65	-33	0 ± 4
J_f	3.190	106.61	-37	-12 ± 2
J_g	3.219	106.10	-37	-13 ± 1
J_h	3.229	109.23	5	31 ± 7

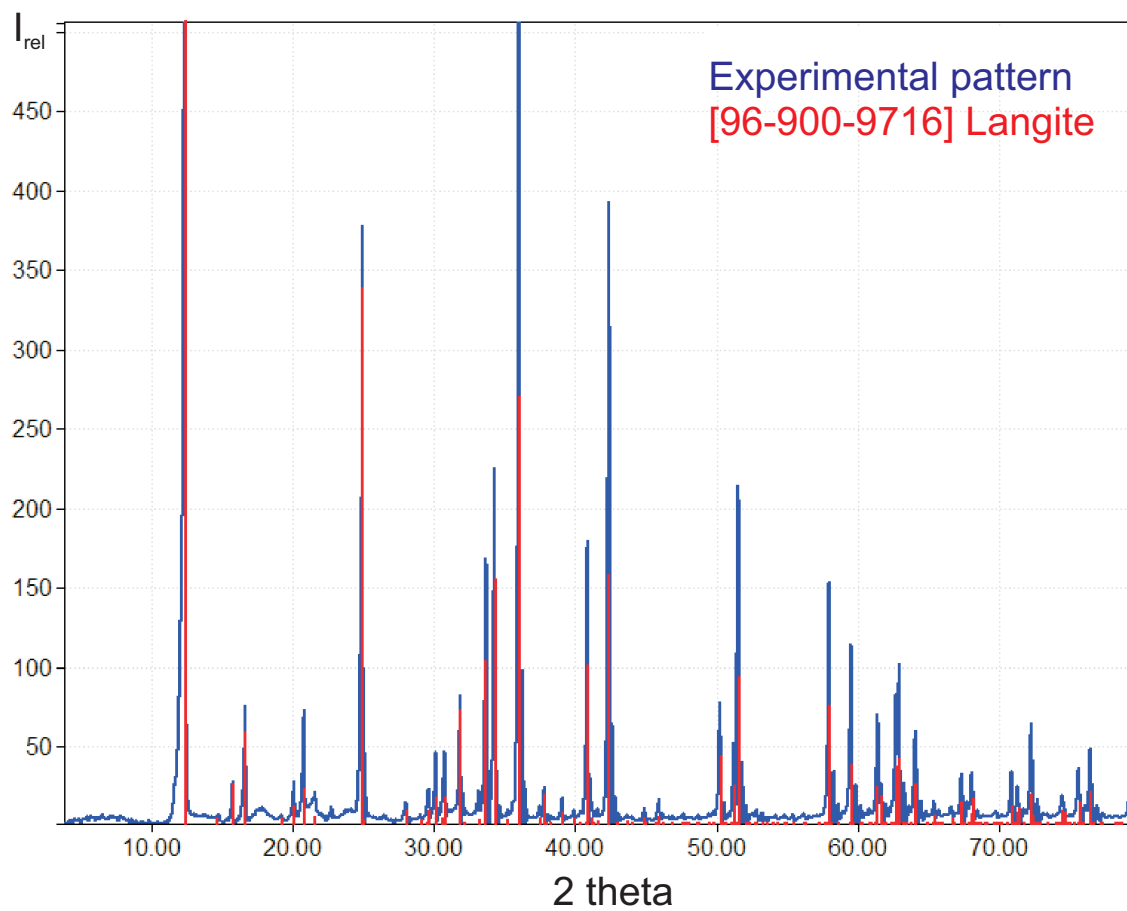


FIG. 7. (Color online) Room temperature powder X-ray diffraction pattern (Huber G670 Guinier camera, $\text{CuK}_{\alpha 1}$ radiation, ImagePlate detector, $2\theta = 3 - 100^\circ$ angle range) of the Langite sample.

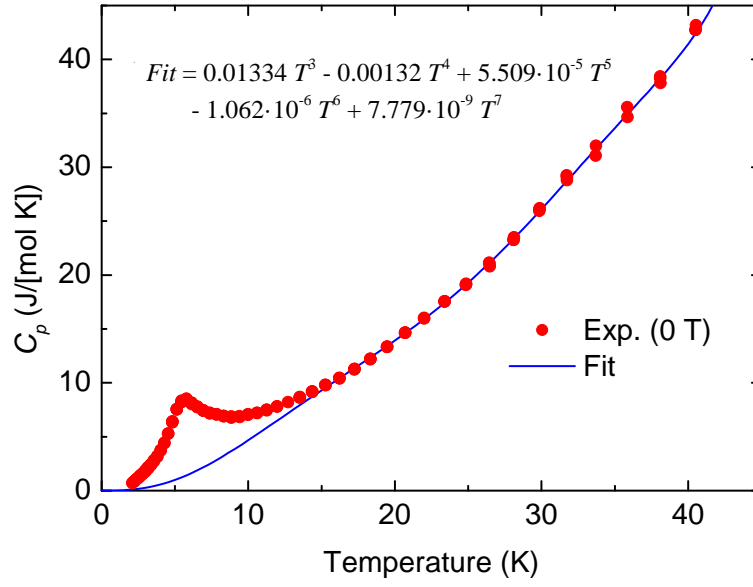


FIG. 8. (Color online) Specific heat data $C_p(T)$ of Langite collected in zero magnetic field. The blue line shows the lattice background $C_{lat}(T)$ which we obtained by fitting a polynomial of the form $C_{lat}(T) = \sum_{n=3}^{n=7} c_n T^n$ to the experimental data in the temperature regime 20–40 K. $C_p(T) - C_{lat}(T)$ yields the magnetic contribution C_{mag} to the specific heat.

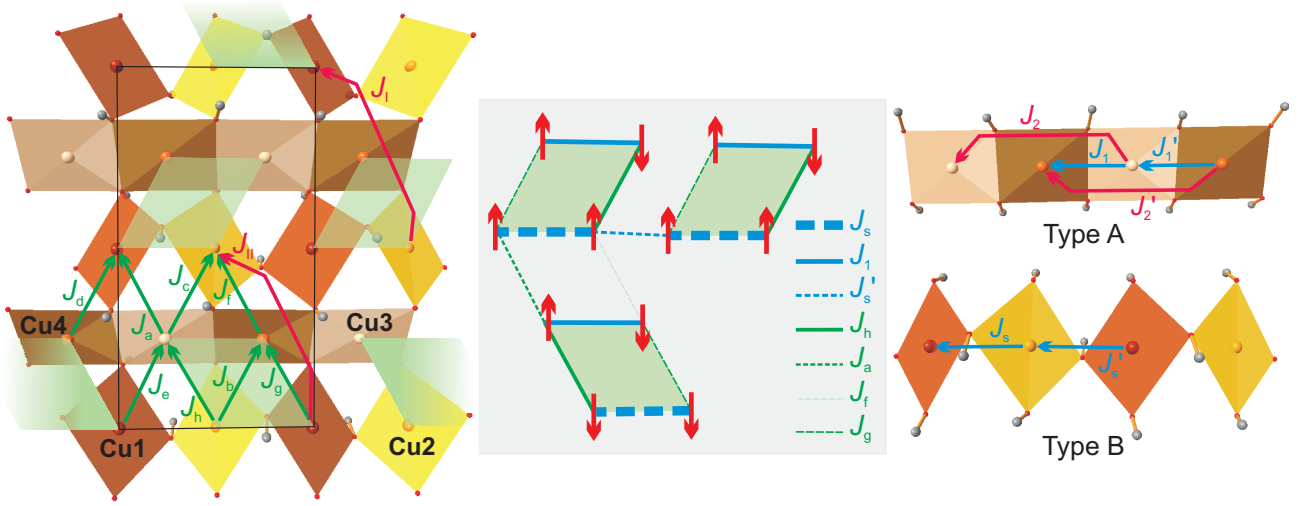


FIG. 9. (Color online) The left panel shows the intralayer exchange pathways. Transparent green areas represent the positions of the $S = 1$ tetramers. These tetramers and the belonging nearest-neighbor J_{ij} are shown in the central graphic where solid and dashed lines indicate AFM and FM interactions, respectively. J_f is depicted in light green color since this coupling is frustrated. The weak couplings J_b and J_d are not displayed. Red arrows indicate the alignment of the $S_z = 1/2$ spins for the isotropic model. The right panel shows the two chain types and the respective intrachain exchange pathways.

Description of the tetramer model

Considering first only the nearest-neighbor couplings (see Fig. 9), an almost unfrustrated microscopic magnetic model for langite is obtained. Only the weak couplings J_b and J_f cannot be satisfied. J_s and J'_s are both FM with J'_s being much smaller than J_s rendering the B-type chains alternating ferromagnetic in this simple model. In the edge-sharing type A chains J_1 is AFM and about four times larger than the weak J'_1 . Thus, the A-type chains can be reduced to AFM Cu3-Cu4 dimers. J_h , reigning between Cu2 and Cu3, couples these dimers to the ferromagnetic B-type chains resulting in $S = 1$ tetramers (central panel in Fig. 9). Cu1 and Cu3 are coupled ferromagnetically by J_a resulting in an antiparallel alignment of the tetramers along c . J'_s , in turn, is responsible for a parallel alignment along the chain direction b . Now, next-nearest neighbor exchanges are taken into account: J_I and J_{II} can be satisfied within the tetramer model but J'_2 and J_2 are frustrated. The model of coupled $S = 1$ tetramers allows the following phenomenological interpretation of $\chi(T)$ and $M(H)$. The bend in $M(H)$, starting at about 10 T, arises from a parallel alignment of the $S = 1$ tetramers in the magnetic field. In this case, 3/4 of the spins are oriented parallel to the magnetic field resulting in a magnetization of $0.5 \mu_B/\text{Cu}$ in agreement with the measurements. The effective AFM coupling between the tetramers J_{it} can roughly be estimated by an AFM $S = 1$ square-lattice spin model yielding $8J_{it}k_B/(g\mu_B) \approx 10$ T and accordingly $J_{it} \approx 1.8$ K. This effective coupling is considerably smaller than our calculated values, e.g. for J_I and J_{II} , however, the seeming discrepancy can be explained by frustration resulting in the very weak effective intertetramer coupling. A similarly small value for J_{it} can be obtained from $\chi(T)$. The maximum of the magnetic susceptibility for an AFM $S = 1$ square-lattice is at about $2.18T/J_{it}$. According to the experimental $\chi(T)_{\text{max}} = 7.5$ K, we, thus, obtain $J_{it} = 3.4$ K. With respect to our crude estimate based on an AFM $S = 1$ square-lattice the agreement between the J_{it} extracted from $\chi(T)$ and $M(H)$ is reasonable and, therefore, justifies the $S = 1$ tetramer model and also clearly shows the crucial role of frustration in langite.

We employ again the tetramer model and assume an intratetramer coupling of about 20–40 K. Now, a saturation field may roughly be estimated using a two-dimensional system with four effective couplings on each Cu-site yielding $4Jk_B/(g\mu_B) \approx 60 - 120$ T. The bend at about 4 T cannot easily be ascribed to certain mechanisms within the phenomenological model but may arise from secondary effects.

The model of coupled tetramers cannot provide a better description of the magnetic properties than the model of coupled magnetic sublattices which we present in the main text. It also neglects the strong NNN J_2 and J'_2 couplings and appears to be counterintuitive since chain features are completely lost. Such feature, however, were observed in neutron experiments on related compounds like brochantite and antlerite (see main text). Therefore, it appears natural to stick to a model based on magnetic chains as long as it is not proved inappropriate.